Technical Note

On Barotropic Response of Arctic Seas to Polar Lows: A Case Study in the Barents Sea

Vladimir Kudryavtsev [1,2], Anastasiia Stokoz [1,*] and Kirill Khvorostovsky [1]

1 Satellite Oceanography Laboratory, Russian State Hydrometeorological University, 195196 St. Petersburg, Russia; kudr@rshu.ru (V.K.); kirill@rshu.ru (K.K.)
2 Marine Hydrophysical Institute RAS, 299011 Sevastopol, Russia
* Correspondence: a.stokoz@rshu.ru

Abstract: In the present paper, we investigate the sea surface height (SSH) anomalies caused by polar lows (PLs) crossing the central part of the Barents Sea and verify if the barotropic response is detectable in the shallow Arctic seas. Analysis of the SSH anomalies in response to the passage of two PLs is performed using satellite altimeter measurements and model simulations. The observed SSH anomalies contained an inverse barometer correction; therefore, they were presumably caused only by the action of surface wind stress in the PLs. The SSH anomalies along the satellite altimeter tracks had the shape of a trough, with the lowest surface height near the center of the PL. The observed anomalies were well distinguished within about one day after the PL passage, with the largest negative value of 0.6 m. The SSH anomalies are analyzed using a simplified model of the ocean barotropic response to the surface wind stress, derived from the hourly wind fields provided in the ERA5 reanalysis dataset. The model quantitatively reproduced the SSH anomalies along most satellite altimeter tracks crossing the PL trajectories. The model simulations revealed that the largest negative SSH anomalies were observed in areas where the PL translation velocity was low and its moving direction changed with the trajectory curvature radius, which was much smaller than the barotropic radius of deformation. The estimated quasi-geostrophic current velocities corresponding to the SSH anomalies in the wakes of the PLs reached 0.15 m/s, which were comparable to the current velocities observed in the Barents Sea.

Keywords: polar low; ocean barotropic response; air-sea interaction; satellite altimetry; sea surface height anomaly

1. Introduction

Polar lows (PLs) are high-latitude, intense, mesoscale cyclones that develop as a result of cold air outbreaks over relatively warm sea surfaces. Despite their comparatively small size of up to 1000 km and short lifetime of a few days, PLs are associated with surface wind speeds exceeding 15 m/s [1] and generate surface waves with heights up to 8–12 m [2], thereby threatening coastal and marine activities.

Although our knowledge about PLs has expanded significantly over the past decades, there are still many unresolved problems, including those related to the processes of atmosphere–ocean interaction. It has been reported that the strong surface winds from PLs may induce intensive upper ocean mixing, leading to positive sea surface temperature anomalies [3], increased depth of deep convection, which impacts large-scale ocean circulation [4], and strengthening of near-surface currents [5].

Sea surface height (SSH) is a key parameter for analysis of the ocean response to moving atmospheric systems. The SSH anomalies resulting from cyclone passage are driven by baroclinic and barotropic ocean responses [6–9] (and references cited therein), which do not interact and can be considered separately [10]. Baroclinic SSH anomalies are inherent to the deep ocean and have been repeatedly observed in studies of the ocean

response to tropical cyclones [11–14]. The barotropic response to tropical and extratropical cyclones has been previously considered over the shelf areas of shallow seas, where its effect is clearly revealed [15–19].

In the present paper, we investigate the SSH anomalies caused by PLs crossing the central part of the Barents Sea and verify if the barotropic response is detectable in the shallow Arctic seas. We evaluate and interpret the spatiotemporal characteristics of the PL-induced SSH anomalies using satellite altimeter measurements and simulations using the simplified model described in [9]. In addition, geostrophic currents generated in the wakes of the PLs are estimated in order to assess their contribution to circulation in the Barents Sea.

The paper is organized as follows: Section 2 describes the data used in the analysis. In Section 3, we present the characteristics of the two PLs considered in this study and analysis of their SSH wakes. Then, in Section 4, we discuss and interpret the observation results. A summary of the results is presented in Section 5.

2. Materials and Methods

2.1. Selected PLs

To investigate the sea surface barotropic response, we selected two PLs observed in the Barents Sea on 19–21 January 2017 and 24–25 November 2018 (hereinafter referred to as PL1 and PL2, respectively). Parameters of these PLs, such as location, size, cloud signature, and stage of development were obtained from the datasets of PLs observed from 1999 to 2019 over the North Atlantic using AVHHR IR images [20,21]. PL1 formed over the deep Norwegian Sea, south of Svalbard, at about 3:00 UTC on 19 January 2017. Until 5:00 UTC on 20 January, it moved eastward to the central part of the Barents Sea, and then it turned to the southeast (Figure 1a). PL2 formed to the west of Novaya Zemlya at about 5:00 UTC on 24 November 2018, moved in the northwest direction in the initial stage of development until 19:00 UTC on 24 November, and then it turned to the southwest (Figure 1b). Both PLs had primarily a comma-shaped cloud signature in the beginning of their lifetimes and acquired a spiral shape during the change of their moving direction.

(**a**)   (**b**)
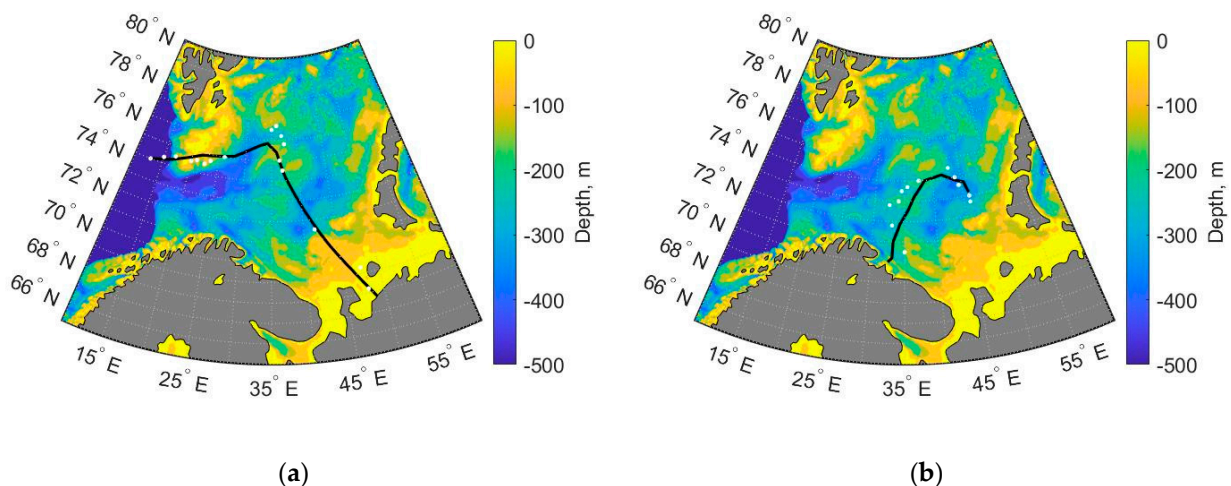
Figure 1. Trajectories of (**a**) PL1 and (**b**) PL2 according to polar low datasets [20] (white dots) and determined from the location of the minimum sea level pressure provided in the ERA5 reanalysis dataset. Trajectories are overlaid on the color map of ocean depth from the GEBCO bathymetric dataset.

2.2. ERA5 Data

The hourly fields of surface wind speed and sea level pressure on regular latitude–longitude grids at 0.25° × 0.25° resolution were obtained from the ERA5 reanalysis dataset [22]. Wind speed fields for the time periods of PL1 and PL2 evolution are shown in Videos S1a and S1b. Sea level pressure data were used to determine PL trajectories using

the location of the pressure minimum (Figure 1). The distances between the PL locations derived from the ERA5 reanalysis dataset and satellite imagery [20] did not exceed the cyclone radius, and we further used the PL trajectories derived from the ERA5 data.

The baroclinic and barotropic ocean responses to a moving cyclone are driven by the vorticity (rotor) of the surface wind stress [6,7]. Along with wind forcing, depression of the atmospheric surface pressure in a cyclone can also affect the barotropic response [6,7]. However, the surface rise caused by this effect is confined within the cyclone area and is effectively removed from altimeter data using the inverse barometer correction (see Section 2.4 for more details). Therefore, we focused only on investigating the effect of wind forcing on SSH anomalies, which is associated with moving wind stress vorticity. The ocean surface wind stress scaled by the water density is defined as:

$$\tau_0 = (\rho_a/\rho_w)C_D u_{10}^2, \tag{1}$$

where ρ_a and ρ_w are the air and water densities, respectively; u_{10} is the 10 m wind speed; and C_D is the surface drag coefficient obtained from the ERA5 data output. Correspondingly, the vorticity of the surface wind stress is defined as:

$$R(x,y) = \partial\tau_y/\partial x - \partial\tau_x/\partial y, \tag{2}$$

where $[\tau_x, \tau_y] = \tau_0[cos\varphi_w, sin\varphi_w]$, φ_w is the wind direction, and τ_0 is defined by Equation (1). Evolution of the surface wind stress vorticity fields for PL1 and PL2 are shown in Videos S2a and S2b, respectively (see also examples in Figures 7 and 8 (column 2)).

2.3. Stratification and Bottom Topography

The vertical cross-sections of the Barents Sea density along the PL1 and PL2 trajectories, derived from the World Ocean Atlas data (WOA18) [23] with a grid resolution of $0.25° \times 0.25°$, are shown in Figure 2. This figure reveals rather weak ocean stratification for the PL evolution periods when the sea water density difference over the pycnocline, $\Delta\rho$, scaled by the mean value, was about $\Delta\rho/\rho = 10^{-3}$, which corresponded to the estimated climatology for the central part of the Barents Sea in November and January.

(**a**) (**b**)
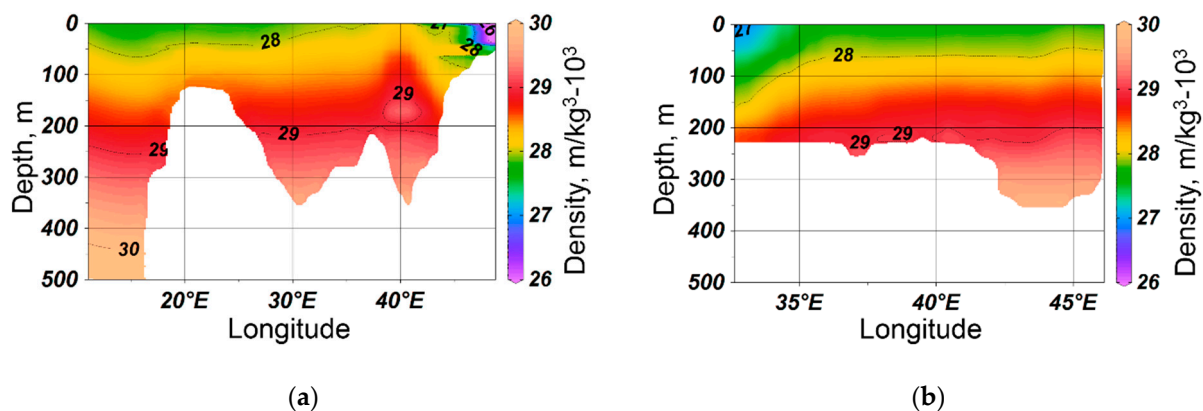
Figure 2. Vertical cross-sections of the Barents Sea density along trajectories of (**a**) PL1 and (**b**) PL2 for the periods of their evolution.

The Barents Sea depth with a spatial resolution of 15 arc-seconds (Figure 1) was taken from the General Bathymetric Chart of the Oceans (GEBCO) dataset [24].

2.4. The Sea Surface Height Anomalies

To investigate the SSH anomalies, we used the Level 2 data of altimeter measurements from the CryoSat-2, Saral, and Sentinel-3 satellites. We utilized the CryoSat-2 Baseline-C Geophysical LRM Ocean Product provided by the European Space Agency (ESA) [25], the Geophysical Data Record—Sea Surface Height Anomaly Saral product derived from AltiKa

altimeter measurements and obtained from the Archiving, Validation, and Interpretation of Satellite Oceanographic (AVISO) data portal [26], and the Sentinel-3 Water product obtained from the European Organization for the Exploitation of Meteorological Satellites (EUMETSAT) [27].

The SSH anomaly estimates provided in these products account for the different tidal effects and those associated with the influence of atmospheric pressure and wind on SSH variations. The effects of atmospheric pressure and wind are included in the Dynamic Atmospheric Correction (DAC), which consists of two parts: the inverse barometer (IB) correction and the high-frequency (HF) wind and pressure response correction. The latter correction is a combination of the high-resolution 2D Gravity Waves Model (MOG2D) [28]), an ocean model forced by ECMWF surface pressure and wind after removing the IB correction. Since the purpose of this paper was to study the barotropic and baroclinic responses of the Barents Sea to PLs using a simplified model tool (see Sections 4.1 and 4.2), we excluded the HF correction from the SSH anomalies and retained only the IB correction. It should also be noted that, unlike the IB correction, the HF correction for the SSH anomalies of the considered PLs was not always available (for example, among eight tracks crossing the PL1 area (Figure 7), the HF correction was available only for one Cryosat-2 track).

Over the period from 19 to 28 January 2017, a total of 116 satellite altimeter tracks crossed the Barents Sea (Figure 3a), but only 27 of them crossed the PL1 trajectory and could be used to indicate the SSH anomalies induced by this PL vortex. Nine tracks crossed the PL1 trajectory within 24 h after the PL passage of the crossing point (Figure 3b), ten tracks passed within the time interval of 24 to 72 h (Figure 3c), and five tracks passed within the time interval of 3 to 6 days (Figure 3d).

(a)　　　　　　　　　　　　　　　　　　　　　　(b)

(c)　　　　　　　　　　　　　　　　　　　　　　(d)
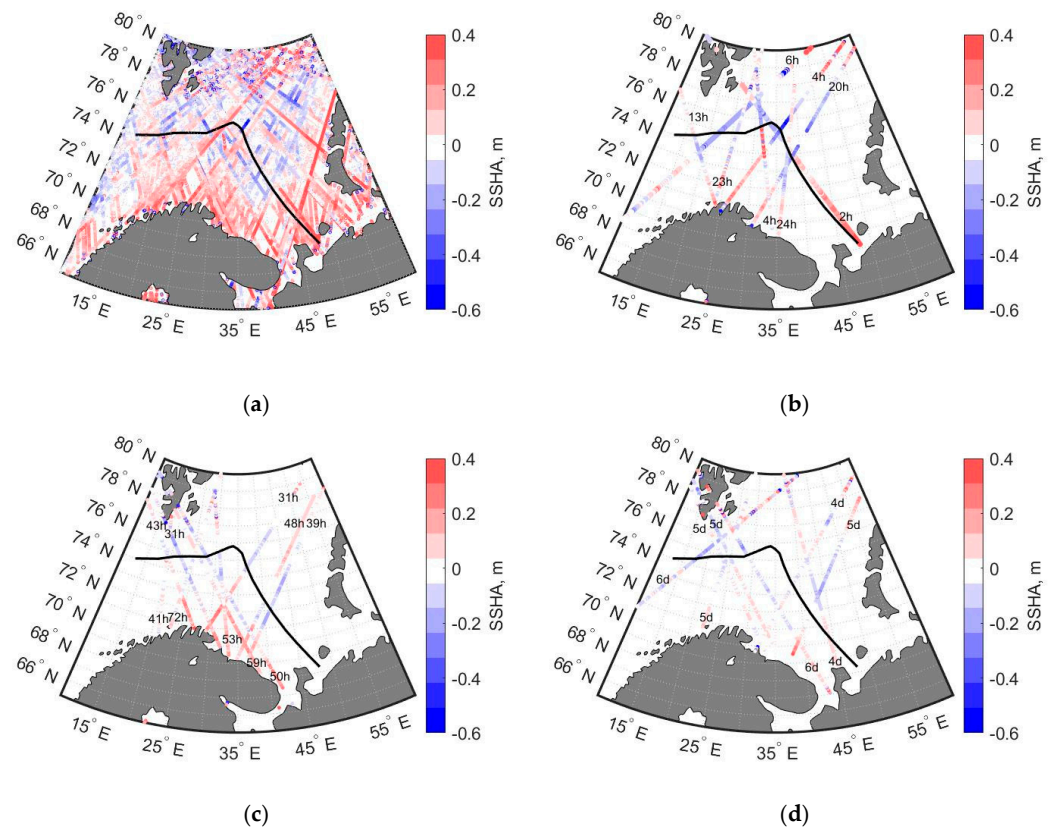
Figure 3. Altimeter tracks from 19 to 28 January 2017 that (**a**) crossed the Barents Sea, and crossed the PL1 trajectory (**b**) within 24 h after the PL1 passage of the crossing point, (**c**) within the time intervals of 24 to 72 h, and (**d**) from 3 to 6 days after the PL1 passage. The color scale indicates SSH anomalies in meters. Solid lines indicate the PL1 trajectory.

To assess the SSH anomalies caused by PL2, we considered only a 4-day period from 24 to 27 November 2018 in order to exclude the impact of the extratropical cyclone that came to the Barents Sea from the North Atlantic, thereby masking the PL effect. During this period, 42 altimeter tracks crossed the Barents Sea (Figure 4a), and only five of them crossed the PL2 trajectory within 24 h after the PL passage of the crossing point (Figure 4b).

(a) (b)
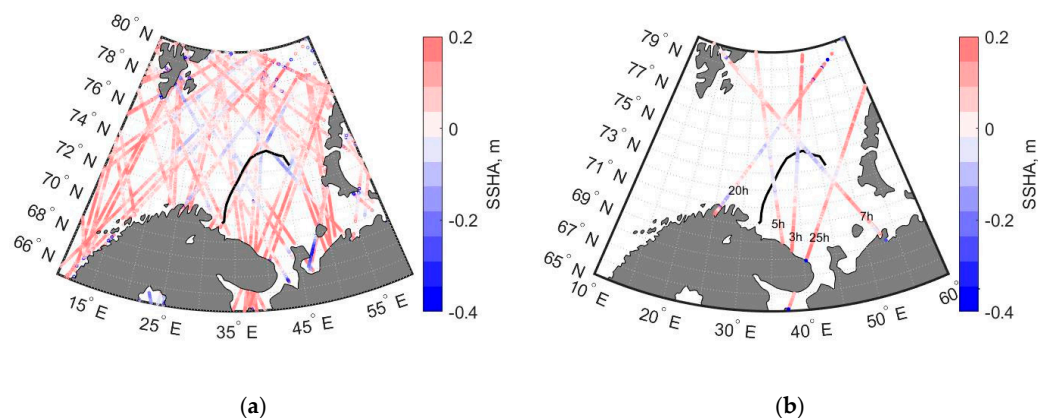
Figure 4. Altimeter tracks from 24 to 26 November 2018 that (**a**) crossed the Barents Sea, and (**b**) crossed the PL2 trajectory within 24 h after the PL2 passage of the crossing point. The color scale indicates SSH anomalies in meters. Solid lines indicate the PL2 trajectory.

The most prominent SSH anomalies caused by the considered PLs were observed within 24 h after their passage (Figures 3b and 4b). For the PL1 case, they varied from 0.4 m in the area outside the cyclone wake to −0.5 m inside the wake. The SSH anomalies gradually decreased with time, varying in the range of −0.4 to 0.2 m in one day, and were hardly visible, although recognizable, in three days. The SSH anomalies induced by PL2 were weaker and varied in the range of −0.2 to 0.2 m.

An example of the SSH anomalies measured by the Sentinel-3 altimeter is shown in Figure 5. The measurements over land as well as those contaminated by the presence of sea ice or rain were removed from the analysis using data flags. As we have noted, the SSH anomaly estimates also accounted for tidal and inverse barometer effects. In addition, it was revealed that due to ocean dynamic processes, the SSH anomalies exceeded the anticipated scale of the PL wakes for most of the altimeter tracks. To remove these large-scale changes, we subtracted the linear trend from the along-track SSH anomalies and further used these corrected data (Figure 5).
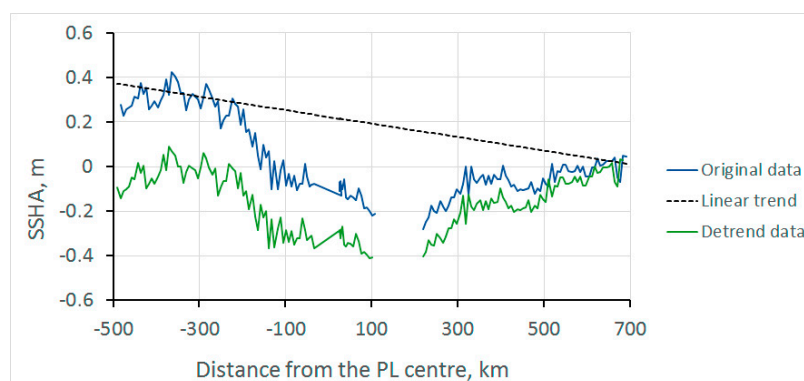

Figure 5. An example of the SSH anomalies obtained from the Sentinel-3 altimeter measurements: the original (blue line) and corrected data after subtracting the along-track linear trend (green line). The dotted black line indicates the linear trend.

3. Results

3.1. Evolution of PLs

The evolution of the maximum surface wind speed, maximum surface wind stress vorticity, and translation velocity of the two considered PLs is shown in Figure 6. At the beginning of PL1 development until about 17:00 UTC on 19 January 2017, the maximum wind speed increased to 27 m/s and then gradually decreased to 22 m/s. Over most of the period of the PL2 lifetime, the maximum wind speed varied in the range of 16–17 m/s and did not exceed 18 m/s. The wind stress vorticity generally followed the evolution of wind speed for both PLs (Figure 6b).
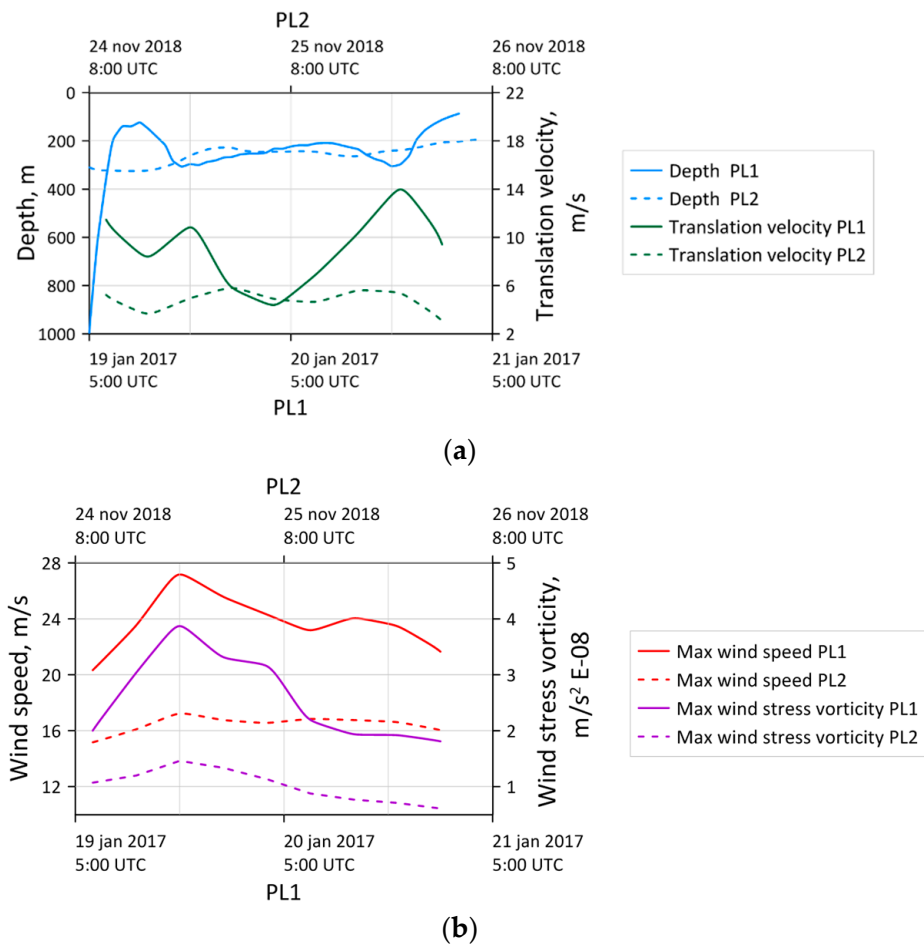
Figure 6. Evolution of (**a**) translation velocity (green lines) and sea depth (blue lines), and (**b**) maximum surface wind speed (brown lines) and maximum surface wind stress vorticity (purple lines) along the PL1 (solid lines) and PL2 (dotted lines) trajectories.

The PL translation velocity (Figure 6a) was calculated using a 5-hour moving average of the PL center location displacement derived from the sea level pressure minimum. The drop in the PL1 translation velocity from 10 to 4 m/s between 17:00 UTC on 19 January 2017 and 4:00 UTC on 20 January 2017 was associated with the change of the PL moving direction from east to southeast (Figure 1a). After the turning point, the PL1 vortex accelerated again to 14 m/s. The PL2 moving direction also changed from the northwest to the southwest within the time interval from 2:00 to 8:00 UTC of 25 November 2018 (Figure 1b), although this was not reflected in the evolution of the translation velocity, which was rather low and ranged from 4 to 6 m/s during the entire PL lifetime (Figure 1a).

3.2. Sea Surface Height Anomalies

To investigate the SSH anomalies induced by the two considered PL vortices, we used satellite altimeter tracks that crossed the PL trajectories within 24 h after the PL passage of the crossing point. In total, eight and six altimeter tracks crossed the trajectories of PL1 and PL2, respectively, within this time interval. Figures 7 and 8 (columns 1 and 2) show these altimeter tracks and the PL trajectories overlaid on the fields of surface wind speed and surface wind stress vorticity corresponding to the time of altimeter measurement. The altimeter measurements (column 4 in Figures 7 and 8) clearly indicated sea surface troughs along most of the satellite tracks, with the lowest SSH near the PL center.

The negative SSH anomalies induced by PL1 increased from 0.2–0.3 m at 18:00–19:00 UTC on 19 January 2017 to about 0.3–0.4 m seven hours later, and the largest value of 0.65 m was measured at about 10:00 UTC on 20 January 2017 (Figure 7). The largest negative SSH anomaly was measured four hours after the PL1 passage and corresponded to the time of the lowest translation velocity observed during the change of the PL moving direction (Figure 6a). Thus, the deepening of the SSH trough in the area of the PL1 turning point could be attributed to an extended period of surface wind stress impact on the sea surface.

The SSH negative anomalies induced by PL2 did not exceed 0.3 m (Figure 8), which was due to the comparatively low surface wind speed and corresponding surface wind stress vorticity (Figure 6b). The largest negative SSH anomalies were measured at 3:28 UTC on 25 November about 5 h after the PL2 passage, which corresponded to the time of the PL heading change, similar to PL1. Therefore, one may suggest that the distinct SSH troughs along the altimeter tracks crossing the PL2 vortex could also be attributed to a prolonged local surface wind stress impact on the SSH due to the PL heading change and low translation velocity observed over the entire PL lifetime.
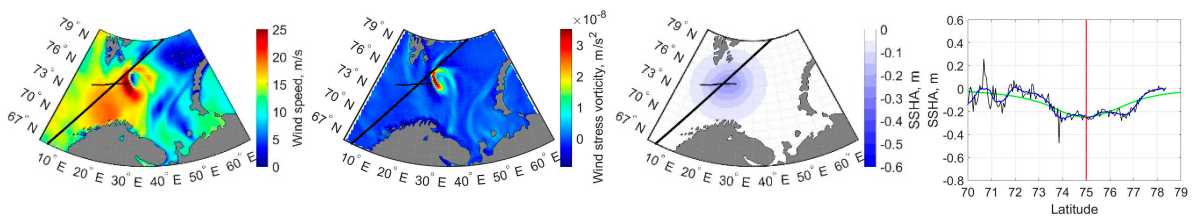
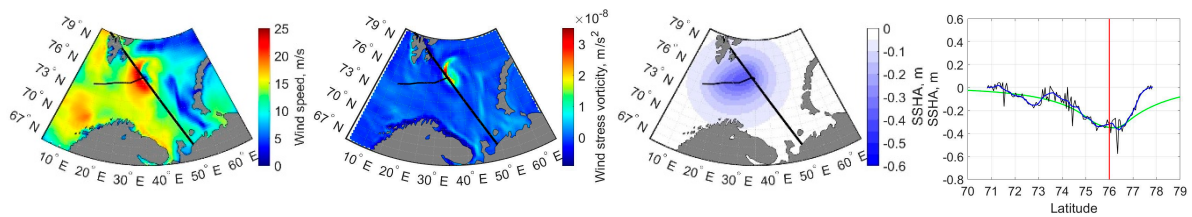Saral: 19 January 2017 17:58 UTC, 6 h after the PL passage
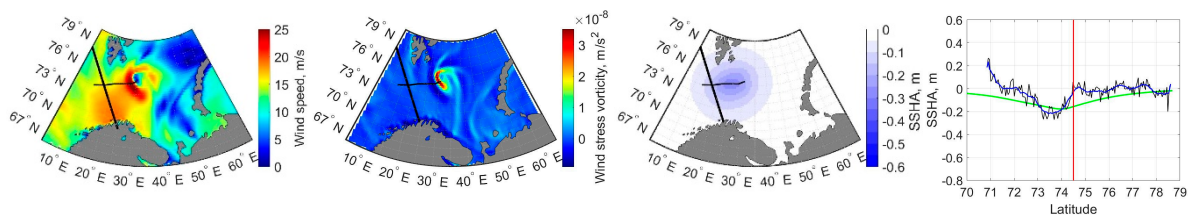
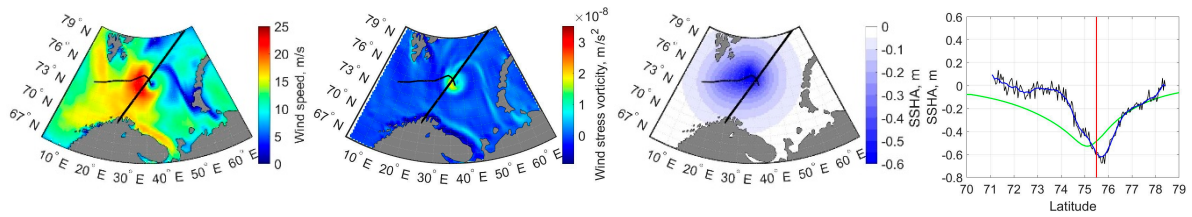Sentinel-3: 19 January 2017 18:43 UTC, 11.6 h after the PL passage
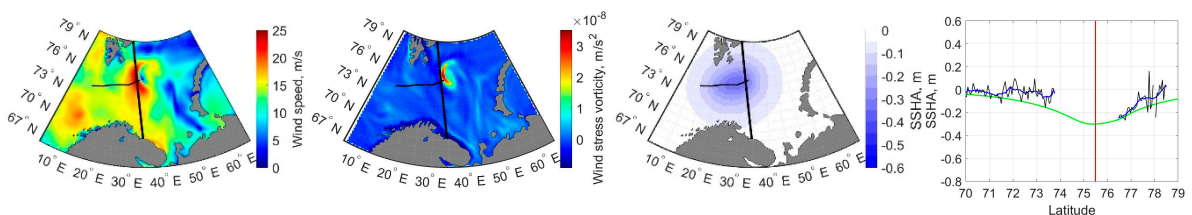
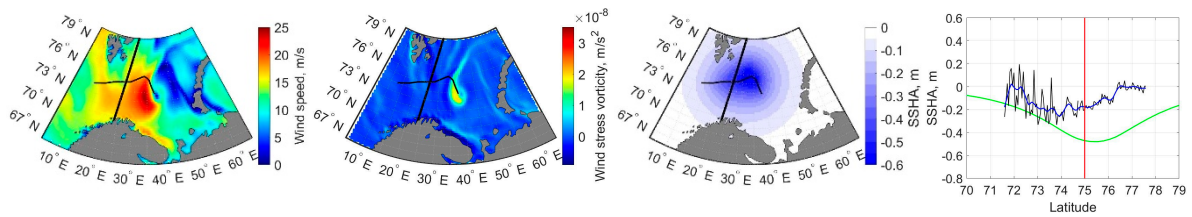Cryosat-2: 20 January 2017 00:34 UTC, 4.5 h after the PL passage
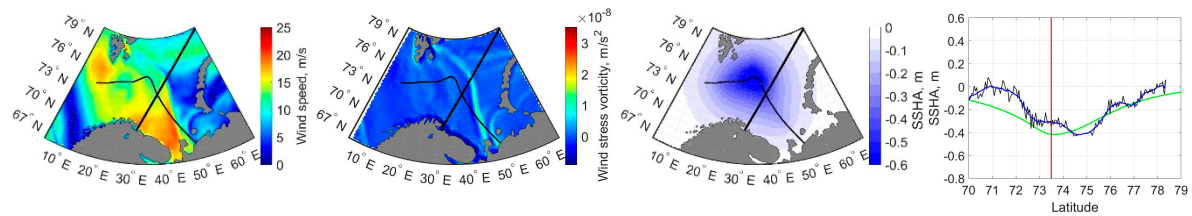
Figure 7. *Cont.*

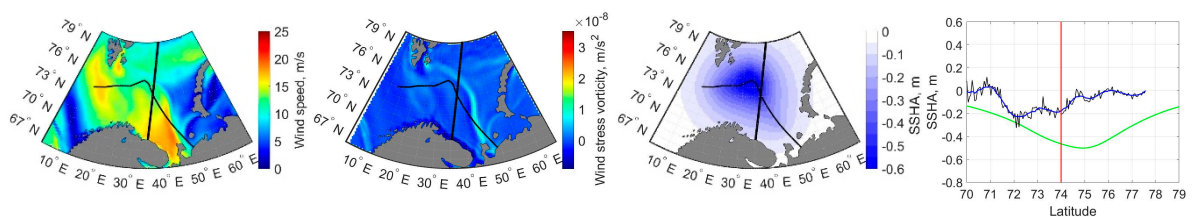Saral: 20 January 2017 01:21 UTC, 2.3 h after the PL passage

Sentinel-3: 20 January 2017 09:57 UTC, 4 h after the PL passage

Cryosat-2: 20 January 2017 13:51 UTC, 22.8 h after the PL passage


Sentinel-3: 21 January 2017 09:31 UTC, 19.5 h after the PL passage

Cryosat-2: 21 January 2017 12:57 UTC, 24 h after the PL passage

Figure 7. (Columns 1 to 3) Altimeter tracks (thick black lines) and part of the PL1 trajectory from the time of PL vortex formation to the time of altimeter measurement (thin black lines) overlaid on the fields of surface wind speed (column 1), surface wind stress vorticity (column 2), and modeled SSH anomalies (column 3) corresponding to the time of altimeter measurement. (Column 4) The SSH anomalies along the satellite track based on altimeter data (black lines), altimeter data using ~7 km running mean (blue lines), and modeling (green lines); the vertical red line on the graphs indicates the position (latitude) where the PL trajectory crosses the altimeter track. The caption under each row provides the time of altimeter measurement and the time difference between satellite track and the PL1 passage at the point where the PL1 trajectory crosses the altimeter track.
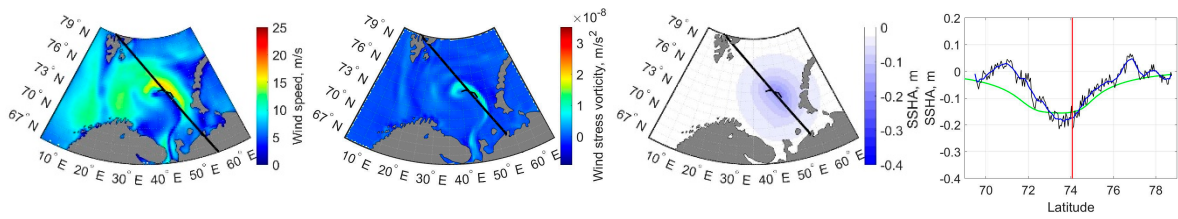
Saral: 25 November 2018 00:38 UTC, 6.6 h after the PL passage
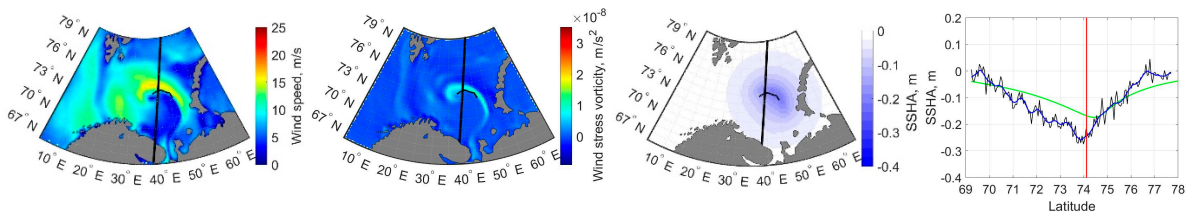
Cryosat-2: 25 November 2018 03:28 UTC, 5.5 h after the PL passage
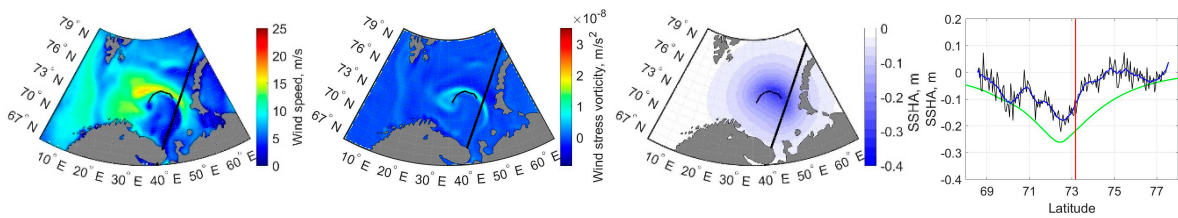
Sentinel-3: 25 November 2018 08:43 UTC, 24.6 h after the PL passage

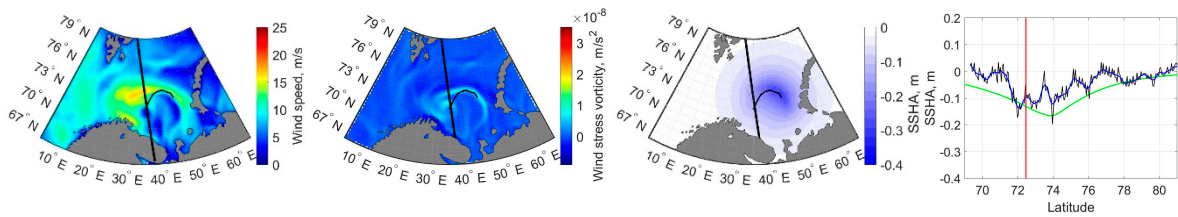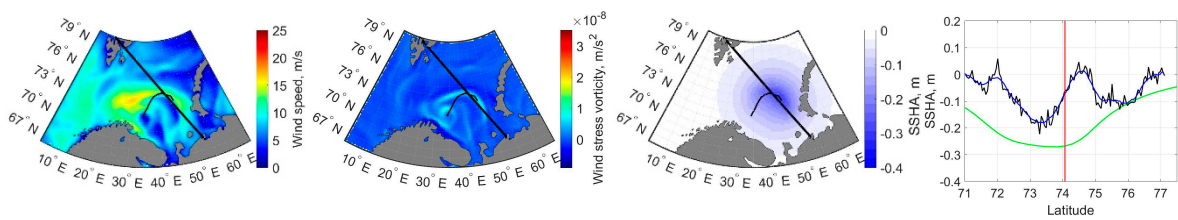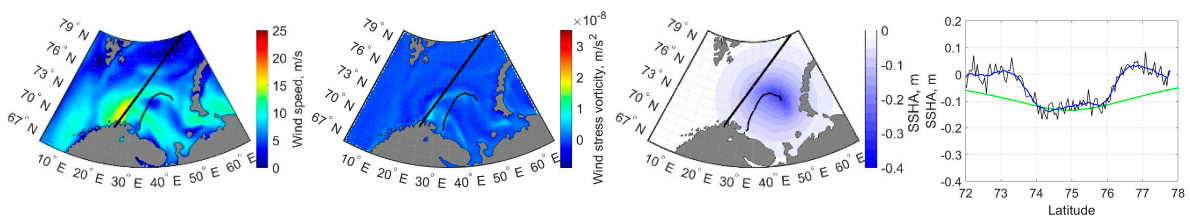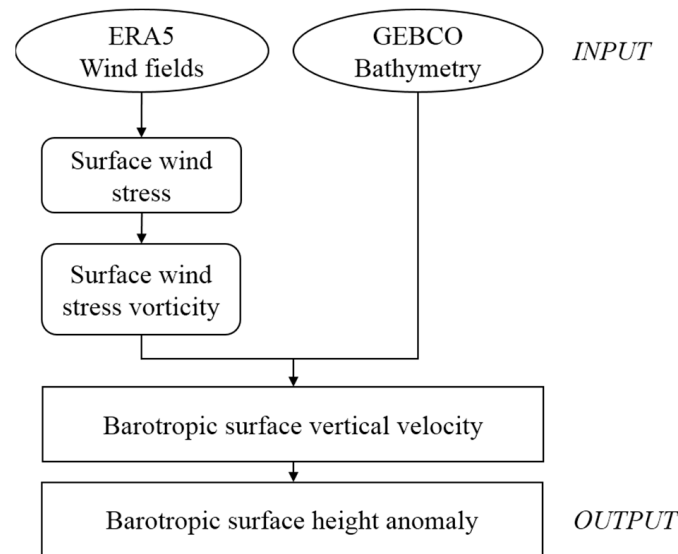Cryosat-2: 25 November 2018 14:57 UTC, 3 h after the PL passage

Sentinel-3: 25 November 2018 17:02 UTC, 23 h after the PL passage

Sentinel-3: 26 November 2018 09:57 UTC, 20 h after the PL passage

Figure 8. The same as in Figure 9 but for PL2.

Figure 9. Flowchart of the model procedure for calculation of the SSH anomalies caused by the barotropic ocean response to the surface wind stress associated with the PL passage.

4. Discussion

To interpret the observed SSH anomalies, we used a simplified model of the baroclinic and barotropic ocean responses to a moving cyclone [9]. The model was based on equations that describe the relationships between ocean vertical velocity and surface wind speed, cyclone translation velocity, ocean stratification, and sea depth.

4.1. Does Baroclinic Response Influence Observations?

The SSH anomalies, δh_s, induced by wind in the moving PL, can be caused by baroclinic, δh_s^{bc}, and barotropic, δh_s^{bt}, ocean responses:

$$\delta h_s = \delta h_s^{bt} + \delta h_s^{bc}. \tag{3}$$

The barotropic response can be considered to be much smaller than the baroclinic one for deep ocean conditions with a depth of about 5–7 km, while in the shallow ocean, the barotropic response is of the same order of magnitude as the baroclinic one [6,10]. The baroclinic response to the PL vortex can be evaluated using the relationship between the surface baroclinic vertical velocity, w_s^{bc}, and the vertical velocity gradient beneath the surface, w_z', invoking the pressure continuity condition at the surface: $w_s^{bc} = -(C^2/g)w_z'$, where C is the phase velocity of long internal waves and g is the acceleration of gravity [9]. Then, the SSH anomalies caused by the baroclinic response, δh_s^{bc}, can be derived in the frame of the two-layer approximation of ocean vertical stratification, as given by:

$$\delta h_s^{bc} = -(C^2/g)\delta D/D, \tag{4}$$

where D is the pycnocline depth and δD is the amplitude of its variations. To derive Equation (4), we evaluated w_z' as $w_z' = w_D/D$, where w_D is the vertical velocity of the pycnocline variation. The amplitude of the pycnocline variation, δD, driven by the surface wind stress vorticity, is proportional to $\tau_{sm}R_m/(CV)$, (Equation (37) in [6]), where V is the cyclone translation velocity; R_m is the radius of maximum wind speed, u_m; and τ_{sm} is the surface wind stress corresponding to u_m. Then, the SSH anomalies induced by the baroclinic response could be estimated using the following equation:

$$g\delta h_s^{bc}/\tau_{sm} = -(C/V)R_m/D, \tag{5}$$

In order to evaluate these anomalies in the study area, we determined the phase velocity of internal waves using an approximation for shallow water [29]:

$$C^2 = g(\Delta\rho/\rho)D(1 - D/H),\tag{6}$$

where $\Delta\rho/\rho$ is the relative density drop in the pycnocline and H is the sea depth. Using typical values for the stratification parameters, i.e., $\Delta\rho/\rho = 10^{-3}$, $D = 100$ m, and $H = 300$ m (see Figure 2), observed values for the PL parameters, i.e., $u_m = 20$ m/s, $R_m = 100$ km, and $V = 4$–10 m/s, and the surface wind stress evaluated as $\tau_{sm} \approx 2 \times 10^{-6}u_m^2$ yielded SSH anomalies caused by the baroclinic response in the range of 0.7 to 1.7 cm. This estimate of the ocean baroclinic response was significantly lower than the troughs measured in the altimeter tracks. Therefore, we interpreted the observed SSH anomalies as the barotropic ocean response to moving PL vortices.

4.2. Barotropic Response: Governing Equations

The barotropic response of the ocean to a moving cyclone can be represented as a sum of the responses to the moving depression of atmospheric pressure and the moving pattern of surface wind stress vorticity [6,7,10]. Although neither response is sensitive to ocean stratification, their effects on SSH anomalies are different. Deformation of the ocean surface (elevation) due to low atmospheric pressure is observed only within the cyclone area and no ridge remains after the PL passage. The effect of the surface wind stress vorticity is preserved after the PL passage, as a SSH trough with respect to the sea surface level is observed before cyclone arrival.

The maximum wind speed radius of about 100 km or less observed for the considered PLs (see Figures 7 and 8) was remarkably smaller than the barotropic radius of deformation, $r_{bt} = C_b/f$, which was about 400 km for the mean sea depth $H = 300$ m, where $C_b^2 = gH$ is the phase velocity of long surface waves. Following Equation (13) in [6] (when $R_m^2 \ll r_{bt}^2$ and $C_b \gg V$), the local sea surface rise due to the depression of atmospheric pressure, ΔP, within the PL area could be assessed as $\xi = \Delta P/(\rho_w g)$. This relationship corresponds to the static response of the sea surface level to atmospheric pressure variations, and it is termed the inverse barometer effect. Since the SSH anomaly estimates provided in satellite altimeter products account for this inverse barometer effect, we attributed the measured height anomalies only to the effect of moving surface wind stress vorticity. An equation for the Fourier component of the surface barotropic vertical velocity in a coordinate system moving with a cyclone in x_1-direction can be written as (Equation (14) in [6]; see also [7,10]):

$$\hat{w}_s^{bt}\left[\left(V^2/C_b^2 - 1\right)k_1^2 - k_2^2 - f^2/C_b^2\right] = f\hat{R}/C_b^2,\tag{7}$$

where hat denotes the Fourier transform; k_1 and k_2 are wavenumber components for the x_1- and x_2-directions, respectively; R is the surface wind stress vorticity defined by (2); and f is the Coriolis parameter. Since $C_b \gg V$, the barotropic vertical velocity can be found directly from Equation (7) using the inverse Fourier transform (Equation (24) in [9]):

$$w_s^{bt} = -f/\left(4\pi^2 gH\right) \iint \hat{R}/\left(k^2 + k_{bt}^2\right)e^{ik_\beta x_\beta}dk_1 dk_2,\tag{8}$$

where $k_{bt} = f/C_b$ is the inverse barotropic radius of deformation. As the term with cyclone translation velocity, V, is ignored, the solution (8) is independent of the orientation of the coordinate system relative to the cyclone heading.

Further, we assumed that the Equation (8) is valid even if the PL translation velocity and heading as well as the surface wind speed and surface wind stress vorticity vary along the PL trajectory. In this case, w_s^{bt} in Equation (8) is considered to be a function "slowly varying" in space and time, $w_s^{bt} = w_s^{bt}(t, x, y)$. Then, the vertical velocity along the PL trajectory could be calculated using the hourly wind fields taken from the ERA5 reanalysis

dataset. The corresponding SSH anomalies were derived by integrating the linear equation $w_s^{bt} = \partial\xi/\partial t$ over time:

$$\xi(x, y, t) = \int_0^T w_s^{bt} dt, \tag{9}$$

where T is the time interval since PL formation and w_s^{bt} is defined by Equation (8). This relationship can also be written by integrating along the PL trajectory:

$$\xi(x, y, t) = \int_0^{L(T)} \left(w_s^{bt}/V \right) dl, \tag{10}$$

where $L(T)$ is the distance traveled by PL since its formation. Equation (9) (or (10)) together with Equation (8) implies larger negative SSH anomalies for shallower seas and slower PL vortices.

It is worth noting that, as discussed in Section 2.4, the effect of wind surface stress (along with the inverse barometer, IB, correction) is initially included in the Dynamic Atmospheric Correction (DAC) of SSH anomalies, termed the high-frequency (HF) wind and pressure response correction. This correction is a combination in the high-resolution 2D Gravity Waves Model (MOG2D, [28]), an ocean model forced by ECMWF surface pressure and wind after removing the IB correction. In its physical meaning, this HF correction describes an effect that is very similar to that modeled by the simplified model described above. However, the HF correction was not available for all of the selected altimeter tracks. Therefore, we simply excluded the HF correction from the SSH anomalies and retained only the IB correction. In this context, the model calculations presented below can be considered as an alternative HF correction to SSH anomalies, although the true purpose of our model simulations was to study the barotropic response of the Arctic seas to PL movement.

4.3. Calculation Procedure

The flowchart of the model procedure for calculating the barotropic ocean response is shown in Figure 9. The ERA5 hourly wind fields and GEBCO bathymetry dataset were used as the input parameters. The surface wind stress and its vorticity were calculated from the wind speed using Equations (1) and (2). In order to exclude the wind impact from the areas outside the wakes of the PL vortices, the surface wind stress vorticity, R, lower than 9×10^{-9} and 6×10^{-9} m/s^2 for PL1 and PL2, respectively, was set to 0. For the model simulations, the sea depth along the PL trajectories was estimated as the sea depth averaged over the area within a radius of 100 km, which approximately corresponded to the radius of maximum wind speed in the PL (Figure 7).

4.4. Simulation Results

The fields of the modeled SSH anomalies caused by the barotropic ocean response are presented in Figures 7 and 8 (column 3) for the time moments corresponding to the selected satellite altimeter tracks and in Video S3a for the entire PL evolution period. In contrast to a moving tropical cyclone, which induces a barotropic SSH wake in the form of a trough along the cyclone quasi-rectilinear trajectory [13,14], the wakes of the PLs considered in this study had rather circle-like shapes. This was because the heading, translation velocity, and maximum wind speed of the PLs varied in time, and the circle-like shapes of the SSH anomaly fields were centered in areas where the effect of the input parameters on the surface vertical velocity was the largest. Nevertheless, the radii of the SSH anomaly circles, representing the widths of the PL wakes, corresponded to the barotropic radius of deformation, $k_{bt}^{-1} = C_b/f$, which was about 350 km for the considered conditions.

The modeled SSH anomalies were generally consistent with the evolution of the PL parameters (Figure 6) and in good agreement with the satellite altimeter measurements along the satellite tracks (column 4 in Figures 7 and 8). In particular, the simulated SSH deepening in the initial stage of PL1 development was associated with the wind speed increase until 17:00 UTC on 19 January 2017 (Figure 6b and Video S3a). Further increase

in the modeled negative SSH anomaly, which resulted from the drop in the translation velocity of PL1 during the change of its heading, quantitatively reproduced the altimeter measurements (Figure 6a, columns 3–4 in Figure 7 and Video S3a). Note that the curvature radius of the PL1 trajectory at the turning point was considerably smaller than the barotropic radius of deformation. This, combined with the low translation velocity, implied a prolonged impact of the PL1 vortex in the area of the turning point, where the circle-like shapes of the SSH anomaly fields were simulated.

The results of the simulation of the barotropic ocean response to PL2 (column 3 in Figure 8 and Video S3b) confirmed that the largest negative SSH anomalies were due to the change of the PL2 heading with a trajectory curvature radius of about 100 km, which was much smaller than the barotropic radius of deformation. Thus, similar to PL1, the change of direction of the slow-moving PL2 vortex caused a long-lasting local impact of the surface wind that resulted in the circle-like shapes of the modeled SSH anomalies.

Although the SSH anomaly measurements and model results were in reasonable agreement, discrepancies for some of the satellite altimeter tracks were revealed. The model underestimated the lowest SSH measured by altimeters on 20 January 2017 at 09:57 UTC (in the PL1 wake) and on 25 November 2018 at 3:28 UTC (in the PL2 wake) by about 0.1 m. As these observations were obtained over areas with the largest sea depth along the PL trajectories, the discrepancies between the measurements and modeled results could be associated with uncertainties in accounting for the bathymetry. Significant SSH model overestimations of measurements along the altimeter tracks on 20 January 2017 at 13:51 UTC and 21 January 2017 at 12:57 UTC (in the PL1 wake) by about 0.2 m, and on 25 November 2018 at 17:02 UTC (in the PL2 wake) by about 0.1 m, could be explained by the large time difference of 23–24 h between the satellite observations and the PL passage. We speculate that this discrepancy was due to hydrodynamic disorganization of the barotropic SSH anomaly fields, which was justified theoretically (see e.g. Section 6 and references in [6]). We also note that the gap in altimeter data due to rain does not permit the comparison of the SSH model simulations with the Cryosat-2 measurements in the vicinity of the PL1 center on 20 January 2017 at 00:34 UTC.

4.5. Barotropic Currents in PL Wakes

The sea surface trough resulting from the barotropic response of the ocean to a moving cyclone represents an element of the upper ocean dynamic system, in which the surface current velocity in the cyclone wake is in geostrophic balance with the SSH anomalies. The components of the quasi-geostrophic current velocity are related to the SSH anomalies as follows:

$$fv = g\partial\xi/\partial x$$
$$fu = -g\partial\xi/\partial y, \tag{11}$$

Figure 10 shows the surface geostrophic currents corresponding to the largest negative SSH anomalies induced by PL1 and PL2 at the final stage of their development. As expected, the streamlines of the quasi-geostrophic current are represented by closed circles. According to the simulated SSH anomalies, the largest current velocities in the barotropic wakes of the PL1 and PL2 vortices reached values of 0.15 and 0.08 m/s, respectively. These estimates were comparable to the current velocities observed in the Barents Sea [30]. Hence, currents resulting from the barotropic response of the ocean to moving PLs may significantly affect circulation in the Barents Sea.

(**a**)   (**b**)
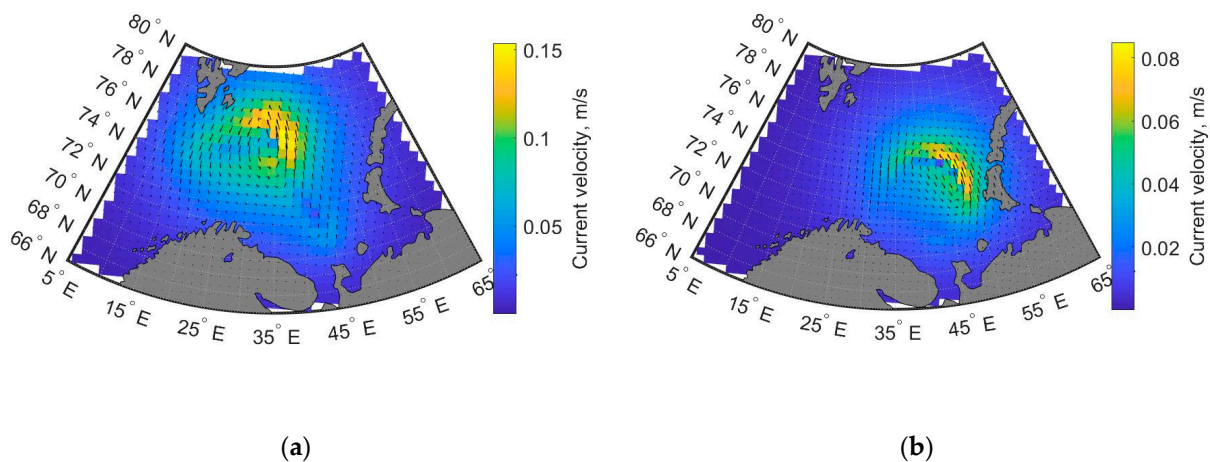
Figure 10. Current velocities estimated by Equation (11) using the modeled SSH anomalies induced by (**a**) PL1 and (**b**) PL2 at the final stage of their development at 00:00 UTC on 21 January 2017 and at 23:00 UTC on 25 November 2018, respectively.

5. Conclusions

The SSH anomalies caused by the passage of two PLs observed in January 2017 and November 2018 in the Barents Sea were analyzed using satellite radar altimetry and model simulations. The inverse barometer correction was taken into account for the SSH anomalies in this study. Therefore, they can be considered as the response of the ocean to "pure" wind forcing associated with moving wind stress vortices. The SSH anomalies in the PL wakes were well detectable by altimeter measurements along satellite tracks as troughs near the center of the PL. The observed SSH anomalies were well distinguished within about one day after the PL passage of the point where the satellite and PL tracks intersected. Over a longer time lag, the SSH troughs were poorly recognizable, presumably due to wake disorganization as a result of dynamic instability, according to theoretical prediction [6]. For the more intense PL1 vortex, with a wind speed higher than 20 m/s during the entire PL lifetime, the largest negative SSH anomalies reached 0.6 m, while for PL2, they did not exceed 0.3 m. For both PL cases, the time of SSH trough deepening corresponded to the change of heading of the slow-moving PL and could be attributed to an extended period of surface wind stress impact on the sea surface.

To interpret the observed SSH anomalies, simplified models of the barotropic and baroclinic responses of the ocean to a moving cyclone were used [9]. We show that the weak ocean stratification observed in the Barents Sea implied insignificant baroclinic SSH anomalies not exceeding 1 cm, which could be neglected in the analysis of the considered PL cases.

The barotropic response in terms of the SSH anomalies was driven by surface wind stress vorticity and was highly dependent on PL translation velocity and sea depth. To derive the surface wind stress fields, we utilized the hourly ERA5 wind speed data as the model input. The results of the model simulations were quantitatively in agreement with the satellite altimeter measurements along most of the satellite altimeter tracks crossing the PL1 and PL2 trajectories. The model simulations confirmed that the largest negative SSH anomalies were observed in areas where the PL heading changed and its translation velocity was low. Furthermore, the curvature radius of the PL trajectories at the turning point was considerably smaller than the barotropic radius of deformation, implying long-lasting local impacts of wind stress, leading to SSH deepening in the PL wakes. Since the PL translation velocity, its moving direction, as well as wind speed varied in time, the wakes of the PLs considered in this study had rather circle-like shapes centered in areas where the effect of input parameters on the surface vertical velocity was the largest, in contrast to tropical cyclones, which induce a SSH wake in the form of a trough along the cyclone trajectory.

To assess the importance of the observed barotropic response for ocean circulation, we estimated the quasi-geostrophic current velocities corresponding to the SSH anomalies observed in the wakes of the PL vortices. The largest current velocities of 0.15 and 0.08 m/s caused by the PL1 and PL2 passages, respectively, were comparable to the current velocities observed in the Barents Sea and may have remarkable impacts on general circulation in this region.

Supplementary Materials: The following supporting information can be downloaded at: https://www.mdpi.com/article/10.3390/rs15174239/s1, Video S1: Evolution of the surface wind speed fields during (a) the PL1 and (b) PL2 lifetime with 1-hour intervals derived from the ERA5 reanalysis dataset. Video S2: Evolution of the surface wind stress vorticity fields during (a) the PL1 and (b) PL2 lifetime with 1-hour intervals. Video S3: Fields of the modeled SSH anomalies with 1-hour intervals induced by (a) PL1 and (b) PL2.

Author Contributions: Conceptualization, V.K.; methodology, V.K. and K.K.; software, V.K. and A.S.; validation, A.S. and K.K.; formal analysis and investigation, V.K., A.S. and K.K.; writing—original draft preparation, A.S.; writing—review and editing, V.K. and K.K.; visualization, A.S.; supervision, V.K. All authors have read and agreed to the published version of the manuscript.

Data Availability Statement: ERA5 reanalysis data are available on the Copernicus Climate Change Service Climate Data Store (https://cds.climate.copernicus.eu (accessed on 15 March 2022)). World Ocean Atlas data (WOA18) are available at https://www.ncei.noaa.gov/products/world-ocean-atlas (accessed on 15 May 2023). The GEBCO bathymetry dataset is available at https://www.gebco.net (accessed on 19 January 2022). CryoSat-2 data are provided by the European Space Agency (ESA) (https://earth.esa.int/ (accessed on 16 February 2023)). AltiKa altimeter measurements are available at the Archiving, Validation and Interpretation of Satellite Oceanographic (AVISO) data portal (http://www.aviso.altimetry.fr/ (accessed on 16 February 2023)). Sentinel-3 data are provided by the European Organization for the Exploitation of Meteorological Satellites (EUMETSAT) (https://archive.eumetsat.int/ (accessed on 12 January 2023)).

Conflicts of Interest: The authors declare no conflict of interest.

References

1. Rasmussen, E.A.; Turner, J. *Polar Lows: Mesoscale Weather Systems in the Polar Regions*; Cambridge University Press: Cambridge, UK, 2003; ISBN 0-521-62430-4.
2. Kudryavtsev, V.; Cheshm Siyahi, V.; Yurovskaya, M.; Chapron, B. On Surface Waves in Arctic Seas. *Bound-Layer Meteorol.* **2023**, *187*, 267–294. [CrossRef]
3. Saetra, O.; Linders, T.; Debernard, J. Can Polar Lows Lead to a Warming of the Ocean Surface? *Tellus A* **2008**, *60*, 141–153. [CrossRef]
4. Condron, A.; Renfrew, I.A. The Impact of Polar Mesoscale Storms on Northeast Atlantic Ocean Circulation. *Nat. Geosci.* **2013**, *6*, 34–37. [CrossRef]
5. Diansky, N.A.; Panasenkova, I.I.; Fomin, V.V. Investigation of the Barents Sea Upper Layer Response to the Polar Low in 1975. *Phys. Oceanogr.* **2019**, *26*, 467–483. [CrossRef]
6. Geisler, J.E. Linear Theory of the Response of a Two Layer Ocean to a Moving Hurricane. *Geophys. Fluid Dyn.* **1970**, *1*, 249–272. [CrossRef]
7. Orlanski, I.; Polinsky, L.J. Ocean Response to Mesoscale Atmospheric Forcing. *Tellus* **1983**, *35A*, 296–323. [CrossRef]
8. Price, J.F.; Sanford, T.B.; Forristall, G.Z. Forced Stage Response to a Moving Hurricane. *J. Phys. Oceanogr.* **1994**, *24*, 233–260. [CrossRef]
9. Kudryavtsev, V.; Monzikova, A.; Combot, C.; Chapron, B.; Reul, N. A Simplified Model for the Baroclinic and Barotropic Ocean Response to Moving Tropical Cyclones: 2. Model and Simulations. *J. Geophys. Res. Oceans* **2019**, *124*, 3462–3485. [CrossRef]
10. Ginis, I.; Sutyrin, G. Hurricane-Generated Depth-Averaged Currents and Sea Surface Elevation. *J. Phys. Oceanogr.* **1995**, *25*, 1218–1242. [CrossRef]
11. Ginis, I. Tropical Cyclone-Ocean Interactions. *Adv. Fluid Mech. Ser.* **2022**, *33*, 83–114.
12. Kudryavtsev, V.; Monzikova, A.; Combot, C.; Chapron, B.; Reul, N.; Quilfen, Y. A Simplified Model for the Baroclinic and Barotropic Ocean Response to Moving Tropical Cyclones: 1. Satellite Observations. *J. Geophys. Res. Oceans* **2019**, *124*, 3446–3461. [CrossRef]

13. Combot, C.; Quilfen, Y.; Mouche, A.; Gourrion, J.; de Boyer Montegut, C.; Chapron, B.; Tournadre, J. Space-Based Observations of Surface Signatures in the Wakes of the 2018 Eastern Pacific Tropical Cyclones. *J. Oper. Oceanogr.* **2020**, *13*, S132–S137.

14. Zhang, B.; Wen, L.; Perrie, W.; Kudryavtsev, V. Satellite Observations of the Sea Surface Height Response to Tropical Cyclones. *Submitt. J. Geophys. Res. Oceans* **2023**. [CrossRef]

15. Fandry, C.B.; Steedman, R.K. Modelling the Dynamics of the Transient, Barotropic Response of Continental Shelf Waters to Tropical Cyclones. *Cont. Shelf Res.* **1994**, *14*, 1723–1750. [CrossRef]

16. Mercer, D.; Sheng, J.; Greatbatch, R.; Bobanović, J. Barotropic Waves Generated by Storms Moving Rapidly over Shallow Water. *J. Geophys. Res.* **2002**, *107*, 3152. [CrossRef]

17. Salcedo-Castro, J.; Ratsimandresy, A.W. Oceanographic Response to the Passage of Hurricanes in Belle Bay, Newfoundland. *Estuar. Coast. Shelf Sci.* **2013**, *133*, 224–234. [CrossRef]

18. Yang, B.; Hou, Y.; Hu, P.; Liu, Z.; Liu, Y. Shallow Ocean Response to Tropical Cyclones Observed on the Continental Shelf of the Northwestern South China Sea. *J. Geophys. Res. Oceans* **2015**, *120*, 3817–3836. [CrossRef]

19. Bezaud, M.; Lazure, P.; Le Cann, B. Wind-Induced Barotropic Oscillations around the Saint Pierre and Miquelon Archipelago (North-West Atlantic). *Cont. Shelf Res.* **2020**, *195*, 104062. [CrossRef]

20. Rojo, M.; Noer, G.; Claud, C. Polar Low Tracks in the Norwegian Sea and the Barents Sea from 1999 until 2019. *PANGAEA* **2019**. [CrossRef]

21. Rojo, M.; Claud, C.; Noer, G.; Carleton, A.M. In Situ Measurements of Surface Winds, Waves, and Sea State in Polar Lows Over the North Atlantic. *J. Geophys. Res. Atmospheres* **2019**, *124*, 700–718. [CrossRef]

22. Copernicus Climate Change Service (C3S) (2017): ERA5: Fifth Generation of ECMWF Atmospheric Reanalyses of the Global Climate. Copernicus Climate Change Service Climate Data Store (CDS). Available online: https://cds.climate.copernicus.eu/cdsapp#!/home (accessed on 15 March 2022).

23. Boyer, T.P.; García, H.E.; Locarnini, R.A.; Zweng, M.M.; Mishonov, A.V.; Reagan, J.R.; Weathers, K.A.; Baranova, O.K.; Paver, C.R.; Seidov, D.; et al. World Ocean Atlas 2018. [Density]. NOAA National Centers for Environmental Information. Dataset. Available online: https://www.ncei.noaa.gov/access/metadata/landing-page/bin/iso?id=gov.noaa.nodc:NCEI-WOA18 (accessed on 15 May 2023).

24. Gridded Bathymetry Data (General Bathymetric Chart of the Oceans). Available online: https://www.gebco.net/data_and_products/gridded_bathymetry_data/ (accessed on 19 January 2022).

25. European Space Agency (ESA). Available online: https://earth.esa.int/ (accessed on 16 February 2023).

26. AVISO+ Satellite Altimetry Data. Available online: http://www.aviso.altimetry.fr/ (accessed on 16 February 2023).

27. EUMETSAT Earth Observation Portal. Available online: https://archive.eumetsat.int/ (accessed on 12 January 2023).

28. Lynch, D.R.; Gray, W.G. A wave equation model for finite element tidal computations. *Comput. Fluids* **1979**, *7*, 207–228. [CrossRef]

29. Phillips, O.M. *The Dynamics of the Upper Ocean*, 2nd ed.; Cambridge University Press: Cambridge, UK, 1977; ISBN 978-0-521-21421-6.

30. Ozhigin, V.; Trofimov, A.; Ivshin, V. The Eastern Basin Water and Currents in the Barents Sea. In Proceedings of the ICES Annual Science Conference, Bruges, Belgium, 30 September 2000.